PHOTONICS Research

Broadband mid-infrared molecular spectroscopy based on passive coherent optical–optical modulated frequency combs

Zhong Zuo,[1,†] Chenglin Gu,[1,3,†] Daowang Peng,[1] Xing Zou,[1] Yuanfeng Di,[1] Lian Zhou,[1] Daping Luo,[1] Yang Liu,[1] and Wenxue Li[1,2,4]

[1]State Key Laboratory of Precision Spectroscopy, East China Normal University, Shanghai 200062, China
[2]Collaborative Innovation Center of Extreme Optics, Shanxi University, Taiyuan 030006, China
[3]e-mail: clgu@lps.ecnu.edu.cn
[4]e-mail: wxli@phy.ecnu.edu.cn

Received 9 February 2021; revised 25 April 2021; accepted 6 May 2021; posted 6 May 2021 (Doc. ID 422397); published 1 July 2021

Mid-infrared dual-comb spectroscopy is of great interest owing to the strong spectroscopic features of trace gases, biological molecules, and solid matter with higher resolution, accuracy, and acquisition speed. However, the prerequisite of achieving high coherence of optical sources with the use of bulk sophisticated control systems prevents their widespread use in field applications. Here we generate a highly mutually coherent dual mid-infrared comb spectrometer based on the optical–optical modulation of a continuous-wave (CW) interband or quantum cascade laser. Mutual coherence was passively achieved without post-data processes or active carrier envelope phase-locking processes. The center wavelength of the generated mid-infrared frequency combs can be flexibly tuned by adjusting the wavelength of the CW seeds. The parallel detection of multiple molecular species, including C_2H_2, CH_4, H_2CO, H_2S, COS, and H_2O, was achieved. This technique provides a stable and robust dual-comb spectrometer that will find nonlaboratory applications including open-path atmospheric gas sensing, industrial process monitoring, and combustion.

https://doi.org/10.1364/PRJ.422397

1. INTRODUCTION

Thanks to their unprecedented frequency accuracy and stability as low as 10^{-18} [1], optical frequency combs (OFCs) have revolutionized optical frequency metrology by linking microwave and optical frequencies [2,3] and have provided new opportunities due to the evenly spaced hundreds of thousands of narrow-linewidth teeth as encountered in molecular spectroscopy [4–6], imaging [7,8], and biochemical research [9]. Several direct frequency comb spectrometers have been developed by combining a single OFC with various methods, such as interferometry [10,11], dispersive elements [12,13], and frequency filtering [14]. Dual-comb spectroscopy (DCS), using two coherent OFCs with slightly different repetition rates, integrates many strengths of conventional Fourier-transform spectroscopy and tunable laser spectroscopy into a single platform [15]. The spectral resolution and accuracy of DCS are only determined by the laser sources rather than the instruments. To date, DCS has innovated many other spectroscopy techniques such as time-resolved spectroscopy [16], coherent Raman spectroscopy [17,18], photoacoustic spectroscopy [19], cavity-enhanced spectroscopy [20,21], and two-photon spectroscopy [22,23]. However, DCS also doubles the challenges of the requirements to the frequency stability of two such OFCs, which can be solved by actively controlling the frequencies of both OFCs, i.e., the repetition frequencies and carrier-envelope offset frequencies, by use a self-reference scheme or a frequency reference to cavity-stabilized continuous-wave (CW) lasers with hertz-level linewidth [24]. The active control processes are generally achieved using phase-locked loops with fast intracavity actuators, such as the current modulation of the pump laser diode, acousto-optic modulators, and piezoelectric transducers [25,26]. Recently, Chen *et al.* devised a novel scheme to achieve mutually coherent DCS using the feed-forward control through an acousto-optic frequency shifter. This scheme gets rid of the modulation of laser cavity and has been demonstrated both in near-infrared and mid-infrared DCS [27–29].

Nowadays, the development of DCS aims at the extension of the wavelength region and the practical applications of DCS in field environments [5,30,31]. Among all the spectral domains, most molecules built the strong fundamental vibrational transitions in the mid-infrared region. However, limited by the gain media, mid-infrared sources are generated mainly based on nonlinear processes, such as difference frequency generation (DFG) sources [32], optical parametric oscillators [33,34],

chip-scale microresonators [35], interband or quantum cascade lasers (ICLs or QCLs) [36,37], and supercontinuum broadened sources [38,39]. Many promising proof-of-principle experiments have demonstrated their intriguing potentials for the generation of mid-infrared DCS. The spectral elements involved in these schemes should be precisely controlled to obtain stabilized mid-infrared comb teeth, but often at the cost of complexity and the demand of a well-maintained laboratory environment. The current trend of achieving fieldable DCS is to design systems with built-in passive mutual coherence, which get rid of the control of a significant freedom, carrier-envelope phase (CEP). The intrapulse DFG or the DFG between two pulse trains sharing common near-infrared oscillators can directly generate mid-infrared DCS with zero-offset CEP [40,41]. Generally, the supercontinuum technique is often implemented to reach the required frequency range for the DFG process. Ycas *et al.* achieved a mid-infrared zero-offset DCS source spanning 2.6–5.2 μm based on the DFG process [42]. Besides, the mode-locked common-cavity oscillators are another choice, which can simultaneously deliver two pulse trains with a stable repetition rate difference [43,44]. However, the direct output spectra cannot reach beyond 3 μm, limited by the gain medium. The slow fluctuations of the cavity length also prevent the long-term stability of the systems. Recently, Nathalie Picqué's group first developed a novel near-infrared DCS via an electro-optic modulation of a common near-infrared CW diode, and then the operating wavelength range was extended into mid-infrared domain by combining DFG process [45,46]. Although the direct output spectral range is limited by the bandwidths of electro-optic modulators (EOMs), the characteristics of the frequency agility and the flat spectral range still attract a great deal of attention. Recently, we achieved a near-infrared DCS via the modulation of a CW laser, which shows good passive mutual coherence with coherent time up to 100 s [47]. To promote the development of fieldable DCS, more efforts should be applied to achieve mid-infrared DCS with a broadband spectral range and robust structure.

In this paper, we develop and demonstrate a broadband mid-infrared DCS based on its built-in passive mutual coherence. By the optical-optical modulation of a CW ICL or QCL, instead of using EOMs [45], the generated optical-optical modulated frequency combs (OMFCs) achieved the output spectral coverage over 400 nm in the mid-infrared domain, and the output power was synchronously amplified to 400 mW in the process. The robust mid-infrared sources have the potential for broadband spectroscopy in the lossy and fieldable environments. Besides, the spectral range of these sources can be tuned flexibly by replacing the operating wavelengths of mid-infrared CW lasers, even to the far-infrared region. The mutual coherence can be well maintained in the full spectral range. The measurements of multiple gas species, including C_2H_2, CH_4, H_2CO, H_2S, COS, and H_2O, were performed to verify the capability and sensitivity for broadband molecular spectroscopy in the experiment. Finally, the frequency accuracy of our mid-infrared DCS was also analyzed for long-term stable operation.

2. PRINCIPLE

Commercial ICLs or QCLs have achieved beam emissions from 2.5 to 24 μm. Mid-infrared OFCs based on multimode operating ICLs or QCLs are investigated to achieve a future integrated comb sensor [35,48]. The number of comb teeth is generally limited to several hundreds, which hinders its applications for broadband and high-resolution spectroscopy. Here we extend the concept of OMFC, proposed in our previous work on near-infrared OMFCs [47] to the mid-infrared region. As shown in Fig. 1, the mid-infrared CW laser is pulsed and amplified by a near-infrared femtosecond pump source in the optical parametric amplification (OPA) process. In the time domain, the CW-seeded OPA process can be explained as the optical–optical modulation process of a CW signal. The modulation frequency is determined by the repetition rate f_{rep} of the pump source. The generated mid-infrared pulses can be expressed as $f_1 = f_{\mathrm{cw}} + n \times f_{\mathrm{rep}}$ (n is an integer), while they are passively referenced to the frequency of the CW laser f_{cw}. Thus, the mid-infrared OMFC is formed without any active CEP control processes once the repetition rate of the pump source is stabilized. The number of comb teeth of the generated OMFCs can reach 10^4 or more. When a common mid-infrared CW QCL is used to generate two OMFCs with slightly different repetition rates, passive mutual coherence between the two mid-infrared combs is achieved. The scheme can be further extended to other wavelength DCS by replacing the operating wavelength of the CW QCL seed. Typically, far-infrared DCS is expected to be obtained by combining appropriate crystals, such as $CdSiP_2$ [48] and OP-GaAs [49].

3. RESULTS AND DISCUSSION

The experimental setup of the mid-infrared DCS is shown in Fig. 2(a). Two near-infrared Yb-doped femtosecond pump sources served as the pump source for the OPA processes, whose repetition rates ($f_{\mathrm{rep1,2}} = \sim$108 MHz) were loosely referenced to a common rubidium (Rb) clock at a low feedback bandwidth of 30 Hz. A tunable CW QCL (3.71–3.9 μm, Daylight, TLS-SK-41038-HHG, less than 5 MHz linewidth for an integration time of 100 ms) or a distributed feedback CW ICL (fixed operating wavelength of 3.37 μm,

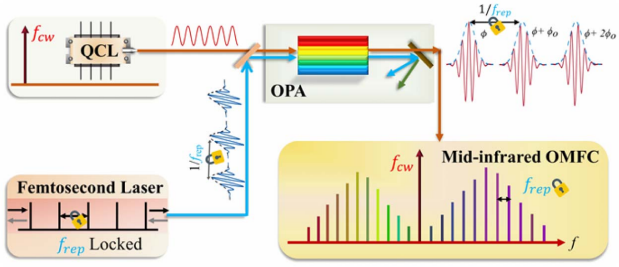

Fig. 1. Schematic of an individual mid-infrared OMFC. A mid-infrared CW ICL/QCL is combined with a near-infrared femtosecond laser, whose repetition rate f_{rep} is locked. Then they are injected into an optical parametric amplifier (OPA). Thus, the mid-infrared OMFC is formed after the OPA process. In the process, the CW signal is pulsed and amplified. The generated mid-infrared pulse sequence inherits the frequency f_{cw} of the ICL/QCL, and its repetition rate is determined by the pump source in the optical frequency domain.

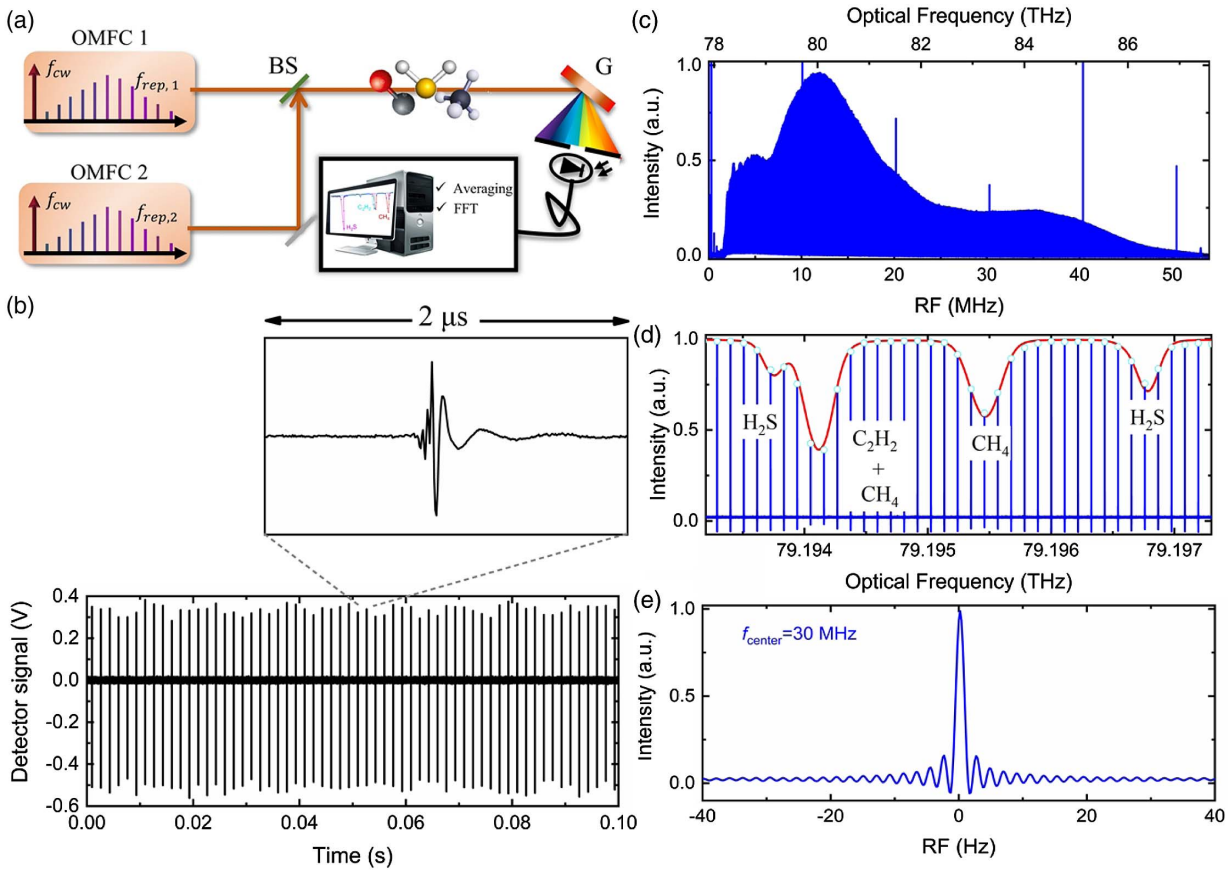

Fig. 2. Mode-resolved DCS spectra. (a) Schematic of the DCS setup. Two OMFCs were combined and then passed through a multipass gas cell. After spectral filtering, the heterodyne signal was detected by a balanced HgCdTe detector retrieved to an optical domain. BS, beam splitter; G, mid-infrared grating. (b) Typical detector signal with multiple interferograms. (c) Retrieved DCS spectrum. One hundred spectra, each with a recording time of ~1 s, were averaged. The top scale is the corresponding optical frequency. (d) Zoomed plot reveals mode-resolved gas absorption lines. The red curve is the gas absorption profile computed from the HITRAN database. (e) Individual comb teeth, centered at 30 MHz in the RF spectrum, show a prefect cardinal-sine shape with an FWHM of 1.4 Hz.

Nanoplus, NP-ICL-3370-TO66-HC, less than 3 MHz linewidth) was used as the seed for mid-infrared comb generation. The CW seed was equally split into two OPAs, which used identical 25 mm long MgO-doped periodically poled lithium niobate (PPLN) crystals (CTL Photonics, fan-out grating, 25.0–30.5 μm). Subsequently, mid-infrared OMFCs were obtained. The output power and spectra obtained directly from the OPAs differed for various crystal periods and CW wavelengths. The maximum output power and spectral coverage exceeded 400 mW and 400 nm, respectively, which enabled the further achievement of supercontinuum broadening in a highly nonlinear fiber (HNLF) or waveguide. More detailed discussions about their noise characteristics and spectral tunability can be found in our previous works [50,51]. To investigate the absorption information of the gas mixture, the two mid-infrared OMFCs were combined and then passed through a multipass gas cell (L_{abs} = 76 m path length, AMAC-76LW from Aerodyne). A balanced HgCdTe detector (QubeDT system) was used to acquire the heterodyne signal, and its output was fed into a 12 bit analogue-to-digital acquisition card (Alazar Tech, ATS9350). To remove the fluctuation of the repetition rate offset of the two OMFCs and obtain the mode-resolved DCS, an adaptive sampling signal, extracted by introducing a CW laser as the frequency intermedium, was used as the external clock to resample the mid-infrared heterodyne signal [48,52]. In addition, experimental works without the adaptive sampling method were also performed. The data acquisition process was triggered by a sharp falling edge of the interferogram, which can be treated as an elementary data phase correction [4,53]. The comparison results with and without the adaptive sampling method showed negligible differences for the spectral measurement of gases at a total pressure of 1 atm as shown in Fig. 7 (Appendix A). This indicates that compared to full-referenced DCS, our DCS without the adaptive sampling method can provide adequate precision for most practical applications in open-path environments (typically at 1 atm pressure), including combustion, exhaust emissions of the engines, and atmospheric monitoring.

To evaluate our mid-infrared DCS, the tunable CW QCL was initially used as the seed, and its operating wavelength was set as 3.85 μm. The repetition rate offset of the pump sources was set to 600 Hz to achieve a single spectral measurement of ~400 nm. An optical filter composed of a mid-infrared reflective diffraction grating and a slit was introduced to adjust the

measured spectral range. A typical detector signal with multiple interferograms is shown in Fig. 2(b). A continuous data stream of 100 s was recorded and then divided into 100 parts. The 100 parts, each with a recording time of 1 s, were averaged. The averaged interferogram was fourfold zero filled to interpolate the spectrum [27]. The spectrum obtained after the Fourier transform without other post-data processes is depicted in Fig. 2(c). The peak signal-to-noise ratio (SNR) was calculated to be 490 at approximately 80 THz. The average SNR across the entire spectrum from 78.2 to 87.6 THz is 180. The figure of merit, defined as $\mathrm{SNR} \times M/T^{1/2}$, is $\sim 1.57 \times 10^6$ $\mathrm{Hz}^{1/2}$, where M (8.7×10^4) is the number of comb teeth and T (100 s) is the measurement time. The noise-equivalent absorption coefficient at 1 s time-averaging per comb line, defined as $(L_{\mathrm{abs}} \times \mathrm{SNR})^{-1}(T/M)^{1/2}$, is $\sim 2.5 \times 10^{-8}$ cm^{-1} $\mathrm{Hz}^{-1/2}$. The enlarged plots in Figs. 2(d) and 2(e) reveal a clear cardinal-sine shape, which is the expected instrumental line shape in a non-apodized spectrum. The dips in Fig. 2(d) represent mode-resolved gas absorption profiles of CH_4, C_2H_2, and H_2S. The spectral resolution, determined by the repetition rates of the pump sources, is 108 MHz. The red curve, computed from the HITRAN database, agrees well with the experimental results. The FWHM of individual heterodyne comb teeth is ~1.4 Hz in the radio-frequency (RF) domain (~250 kHz in the optical domain), which indicates the mutual coherence between our OMFCs.

Figure 3(a) shows a typical optical spectrum retrieved from a single interferogram coherently averaged at $N_{\mathrm{ave}} = 240{,}000$ times when the wavelength of the QCL was 3.72 μm. Here the repetition rate offset of the pump sources was set as 2.4 kHz, and the nonaliasing spectral range was ~100 nm. The multipass gas cell was filled with a gas mixture (1.7%CH_4, 2.2%C_2H_2, and 5.5%H_2S) in N_2 buffer gas at a total pressure of 4 mbar. The overall background spectrum was removed by fitting the spectral baseline to extract the gas absorption lines as shown in Fig. 3(b). The theoretical results of different gases from the HITRAN database are represented using different color curves. All the absorption lines from CH_4, C_2H_2, and H_2S are consistent with the theoretical profiles as shown in Figs. 3(c)–3(f). The FWHM of the Doppler-broadened

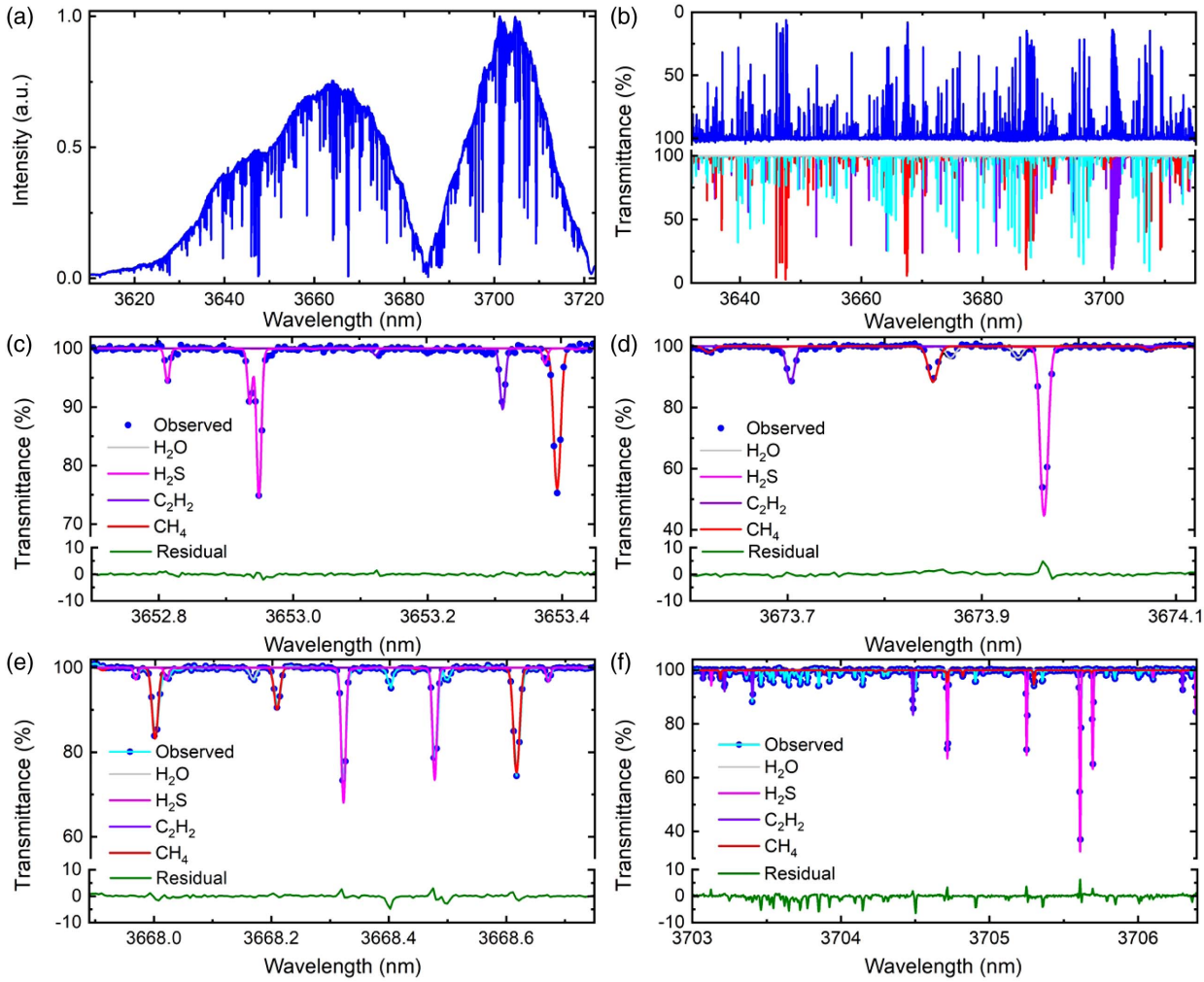

Fig. 3. DCS spectra of a mixture of gases. (a) Optical spectrum retrieved from a single interferogram coherently averaged 240,000 times. (b) Comparison results of the extracted gas absorption lines (blue line) and the theoretical profiles from the HITRAN database (light grey curve for H_2O, magenta curve for H_2S, violet curve for C_2H_2, and red curve for CH_4). (c)–(f) Portions of the gas absorption lines of (b). The olive scatter represents the residual between the measured results and absorption profiles of these four gases from the HITRAN database.

rovibrational lines is ~250 MHz. After comparison with the theoretical profiles, the concentrations and compositions of the gas mixture can be derived. All the absorption lines from H_2O in the measured spectral range can be observed, which could be attributed to the residual water vapor in the gas cell. The concentration of H_2O was calculated to be 6%, according to the gas absorption strength. There are some unexpected absorption lines that cannot be inferred from the open gas information of the HITRAN database. Portions of the unknown gas absorption lines, which may originate from impurities in the gas mixture, are shown in Figs. 3(e) and 3(f). The experimental results demonstrate the full potential of our DCS system for the quantitative analysis of gas species and concentrations.

Our mid-infrared DCS has the well spectral tunability by adjusting the PPLN periods or the operating wavelength of the common CW laser. As shown in Fig. 4, a spectral coverage

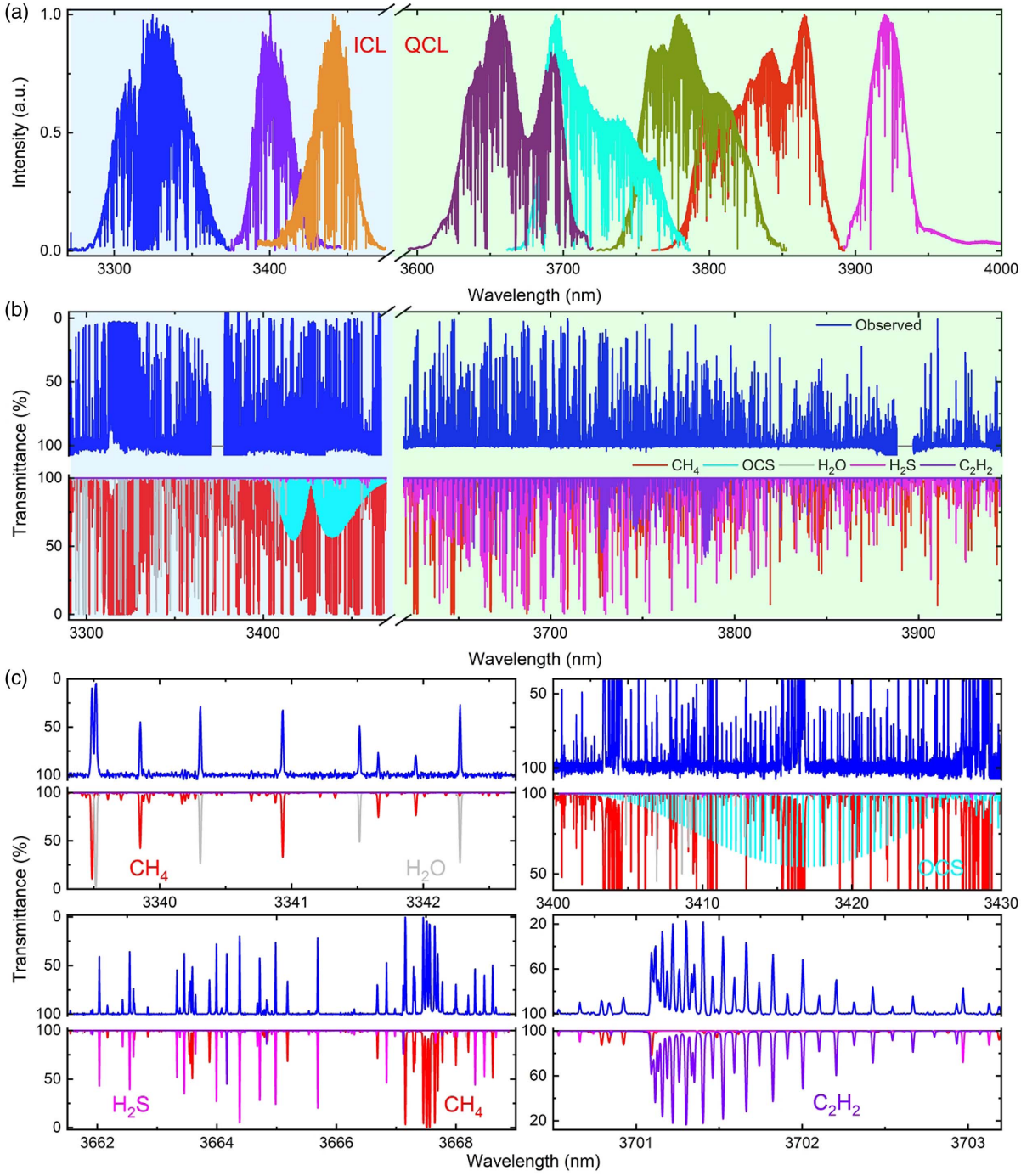

Fig. 4. Tunable DCS spectra. (a) Measured spectra by scanning PPLN periods and adjusting the operating wavelength of the common CW laser. (b) Comparison between extracted gas absorption lines of (a) and the theoretical gas absorption profiles from the HITRAN database. The gaps are due to the electronical filter with a bandwidth of 2–48 MHz in the data acquisition processes. The weak spectral intensity and the low-frequency noises of the mid-infrared detector result in the deviations of the absorption intensity near the two gaps. (c) Portions of gas absorption lines of five gases.

ranging nearly from 3.3 to 4.0 μm was achieved by stitching the measured DCS spectra, each of which was averaged in a time of 100 s. Here the DCS spectra seeded by QCL were measured mainly by adjusting the operating wavelength of the CW laser at a step of ~50 nm. For the ICL seed operating at a fixed wavelength of 3.37 μm, the spectral tuning was achieved by scanning the crystal periods. Owing to the low injected CW power of ~5 mW of the ICL, the relative intensity noise increased dramatically for the parameter fluorescence in the OPA processes [54]. This resulted in the degradation of the spectral SNR compared to that of the QCL seed, whose injected power is usually ~100 mW. The violet curve in Fig. 4(a) shows a figure of merit of $\sim 4.1 \times 10^5$ from 3.38 to 3.43 μm. The mode-resolved spectra at different frequency regions are shown in Fig. 8 (Appendix B), revealing the good mutual coherence of our OMFCs. The extracted gas absorption lines obtained when the gas cell is filled with the molecular gases C_2H_2, CH_4, and H_2S at a total pressure of 10 mbar are shown in Fig. 4(b). Portions of different gas absorption lines are shown in Fig. 4(c). The unexpected absorption lines of rare COS, which is generally treated as an impurity in the gas mixture, are observed near 3.45 μm. The components of the gas mixture were estimated to be 0.55% C_2H_2, 1.6% CH_4, 5% H_2S, 6% H_2O, and 0.014% COS. By introducing well-designed chirped PPLN waveguides, broadband mid-infrared sources can be directly obtained by improving the phase-match bandwidth [55]. A preliminary experimental result demonstrated a mid-infrared source ranging from 1.8 to 4.2 μm as shown in Fig. 9 (Appendix C), in which a chirped PPLN crystal with a 25 mm length was used. These results demonstrate the potential of our scheme for octave-spanning mid-infrared DCS.

Mid-infrared DCS can be used for highly sensitive molecular detection owing to the strong rovibrational absorption lines. Here we used our DCS to detect H_2CO gas (which is one of the main harmful gases) with parts-per-million (ppm)-level concentration. High levels of exposure to H_2CO can cause cancers as announced by the US Department of Health and Human Services in 2011 [56]. The World Health Organization (WHO) set an indoor air permissible concentration value of 0.08 ppm (0.1 mg/m^3) of H_2CO for all 30 min periods lifelong in 2010 [57]. In the experiment, the gas cell with a path length of 76 m was filled with 2.5 ppm H_2CO at a total pressure of 83 mbar. As shown in Fig. 5(a), the DCS spectrum, filtered by adjusting the slit before the mid-infrared detector, was measured with an average time of 10 s. In Fig. 5(b), the maximum absorption intensity of the extracted absorption lines was ~10%, and these absorption lines agree well with the theoretical results. The standard deviation of the residuals, limited by the residual baseline fluctuations in the retrieved spectrum, is ~0.32%. The $1-\sigma$ sensitivity of H_2CO is considered as the concentration level when the absorption intensity of absorption lines in the measurement spectral region equals the value of ~0.32% [5]. According to the simulation results in open-path environments, the $1-\sigma$ sensitivity of H_2CO is calculated to be ~0.04 ppm in a measurement time of 10 s, which is lower than the permission concentration level of 0.08 ppm. Moreover, narrowing the measured spectral range or increasing the measurement time

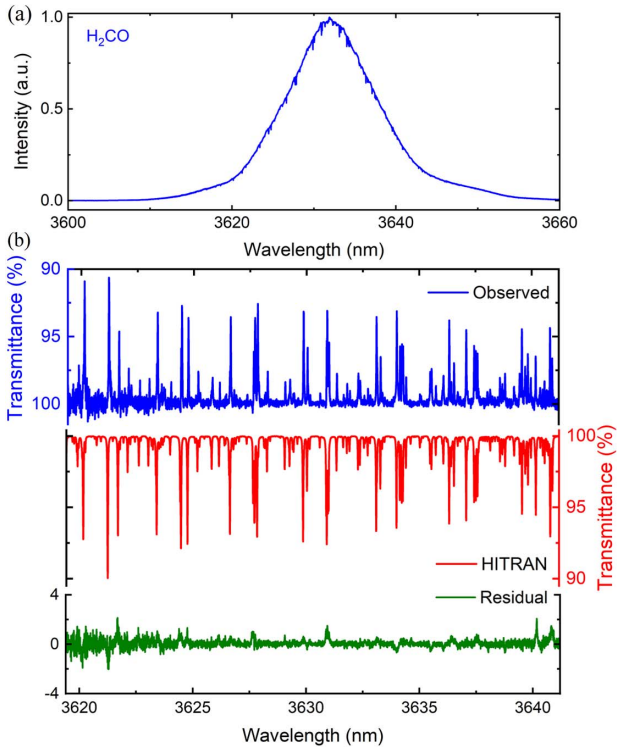

Fig. 5. DCS spectra of H_2CO at a ppm-level concentration. (a) Retrieved DCS spectra of H_2CO. (b) Comparison between the measured results and theoretical profile from the HITRAN database. The standard deviation of the residual is ~0.32%.

can further improve the sensitivity due to the higher SNRs. These results demonstrate the potential of our mid-infrared DCS for the sensitive measurement of harmful gases.

In the experiment, the commercial CW ICL/QCL was kept relatively stable by controlling the operating current and temperature. The frequency fluctuations of the CW seeds result in the entire frequency shift of the mid-infrared OMFCs, which also mainly influences the frequency accuracy of our DCS. In this study, we used a mid-infrared wavelength meter (Bristol 771B, 0.75 pm accuracy) to measure the optical frequency of the CW seeds. The standard deviation of the frequency fluctuations of the QCL was ~3.5 MHz, recorded with a single measurement time of ~0.4 s and a total measurement time of 30 min, whereas that of the ICL was ~5.0 MHz, as shown in Fig. 10 (Appendix D). The measured results are comparable to those of the frequency accuracy of the wavelength meter, which was assessed by measuring the frequency of a narrow-linewidth near-infrared CW diode (1560 nm, OEwaves, linewidth ~10 Hz) referenced to an Er-doped fiber comb based on an f-$2f$ structure [26]. If necessary, the mid-infrared CW laser can be further referenced to an optical clock or a stabilized frequency comb [24]. For further evaluation of the influence of our CW frequency shifts on the absorption spectrum measurement, the portion of absorption lines of the gas mixture of C_2H_2, CH_4, and H_2S was properly fitted to extract the center frequency as shown in Fig. 6(a). The total pressure of the 76 m multipass cell was 10 mbar at 296 K. The residual between the measured spectrum and its fit has a standard deviation of 0.7%,

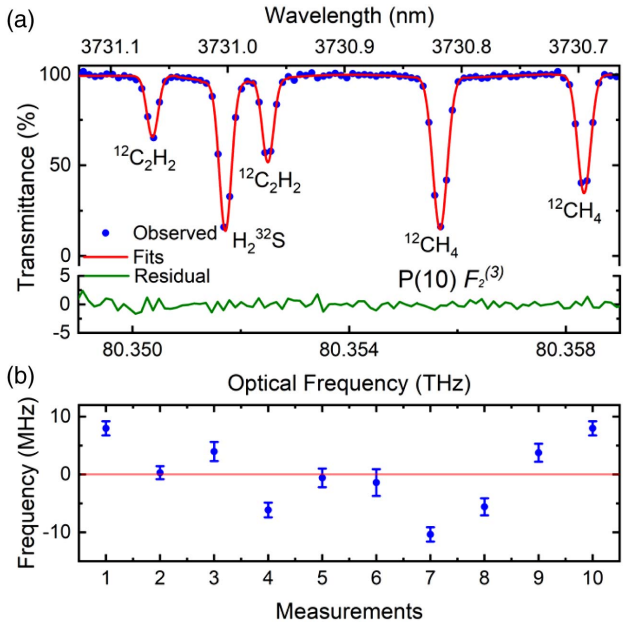

Fig. 6. Line parameter measurements. (a) Portions of the gas absorption lines of the gas mixture of C_2H_2, CH_4, H_2S. Gaussian profiles (red curves) are used to fit the measured results (blue dots). The standard deviation of the residual between the measurement and its fit is calculated to be ~0.7%, which includes the statistical and residual baseline noise. (b) Statistical distribution of 10 continuous measurements of the $^{12}CH_4$ P(10)$F_2^{(3)}$ line center frequency. The error bar of each measurement is the standard error of the fitted line position parameter. The horizontal red line represents the average center frequency (80,355,670.1 MHz), which has been subtracted from each measured frequency for clarity.

which shows a good agreement. The optical frequency was retrieved from the RF domain according to the CW frequency calibrated by the center frequency of one of the gas absorption lines and the repetition rates referenced to a Rb clock. The statistical distribution of 10 continuous frequency measurements for the $^{12}CH_4$ P(10)$F_2^{(3)}$ line position is shown in Fig. 6(b), in which the CW frequency was treated as a constant in the total measurement time of 100 s. The measured statistical uncertainty of the center frequency is ~6.1 MHz. For the Gaussian fit, the inherent fit uncertainty of the center of the gas absorption lines can be theoretically expressed as $\sigma_f = \Delta\nu_{\mathrm{FWHM}}/(\mathrm{SNR} \times \sqrt{N_{\mathrm{pnt}}})$, where $\Delta\nu_{\mathrm{FWHM}} = \sim 300$ MHz is the FWHM of P(10)$F_2^{(3)}$ and $N_{\mathrm{pnt}} = \Delta\nu_{\mathrm{FWHM}}/f_{r,s}$ is the number of measured points across the FWHM [40,58]. The value is calculated to be $\sigma_f = 0.79$ MHz for the gas absorption line P(10)$F_2^{(3)}$. The SNR and $f_{r,s}$ (repetition rate of OMFC) are 220 and 108 MHz, respectively. Compared to the FWHM of the absorption lines P(10)$F_2^{(3)}$, which is slightly broader than the Doppler-broadened linewidth of ~275 MHz, the influence of CW frequency shift on the measurements of gas concentration and components can be negligible in our experiment. On the other hand, the continuous operation testing in a combustion lab demonstrated the practical applications of our DCS in industrial environments as shown in Visualization 1. The studies of the field-programmable gate array (FPGA) real-time averaging of our DCS were also carried out. These results have highlighted the full potential of our OMFC concept for future compact mid-infrared DCS sensors for nonlaboratory applications.

4. CONCLUSION

We proposed and demonstrated a broad mid-infrared DCS based on the OMFC technique, passively referenced to a common commercial CW QCL or ICL. Mutual coherence was established without any fast feedback circuits or post-phase corrections, which is favorable for simplifying the architecture and improving the robustness of the DCS. The direct output spectral range reached several hundred nanometers with an average output power exceeding several hundred milliwatts (mW), which can be applied in nonlinear spectroscopy or lossy measurement environments. By introducing a PPLN waveguide, an octave-spanning spectrum is expected to be achieved. Furthermore, the scheme can be extended to the far-infrared region, whereas the OMFC concept has been demonstrated in the near-infrared domain [48]. On the other hand, the measurements of multiple gas species such as H_2CO at a ppm concentration were performed. The long-term stability, high-spectral SNR, and rapid measurement capacity of our DCS were effectively verified, which equal or exceed the high-performance mid-infrared Fourier-transform spectrometers [10,15,59]. With continued development, we anticipate that our optical–optical-modulated DCS with high robustness, coherence, and stability will become a deployable spectroscopic tool offering great resolution and sensitivity in fundamental physics studies and field applications in the future.

APPENDIX A: REAL-TIME COHERENT AVERAGING

Real-time coherent averaging was performed based on an FPGA module. The data acquisition process was triggered by a sharp falling edge of the interferogram to remove the possible time jitter, which can be treated as an elementary phase correction [53]. As shown in Visualization 1, the refresh rate is determined by the coherent averaging number and repetition rate difference of our DCS. Typically, the refresh rate can exceed kilohertz (kHz), and the single measured spectral range can reach several hundred nanometers. This surpasses traditional spectral measurement techniques, such as Fourier-transform spectrometry. As shown in Figs. 7(a)–7(c), the comparative results with and without the adaptive sampling method showed little difference for the measurement of 10% CH_4 at a total pressure of 1 atm and an optical path length of 30 cm. This result indicates that our DCS without the adaptive sampling method is precise enough for most practical spectral measurements usually performed in a field environment (1 atm pressure). The averaging result obtained by the FPGA module with a total time of 1 h exhibits an expected evolution of the average SNR with time as shown in Fig. 7(d). No saturation in the trend of the increasing SNR was observed. These results demonstrate the potential of our OFMCs for compact, robust, and deployable mid-infrared DCS in the future.

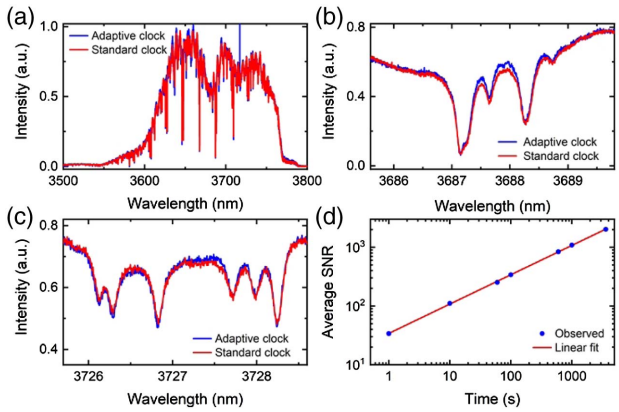

Fig. 7. (a) Comparison of results with and without the adaptive sampling method at a measurement time of 10 s. A 30 cm optical path cell is filled with 10% CH_4 in N_2 buffer gas at 1 atm pressure. The standard clock indicates that the constant internal clock of data acquisition card served as the acquisition clock. (b), (c) Zoomed plots of (a) reveal the little difference between the two results. (d) Evolution of the average spectral SNR as a function of the measurement time without the adaptive sampling clock. The FPGA module triggered by the falling edge of the interferograms exported the data files at time intervals ~1 s. Each file represents the averaged results of 600 interferograms. In the experiment, 3600 files, including 3600 × 600 interferograms, were obtained and then averaged. A power law fit with an exponent of 0.499(3) indicates that the SNR is proportional to the square root of the measurement time, which is expected for coherent averaging.

APPENDIX B: MID-INFRARED FREQUENCY-AGILE DCS

To verify the frequency agility of our OMFCs, the original streams at different injected CW wavelengths as shown in Fig. 4, in which the adaptive sampling signal was used as the external clock of the acquisition card, were divided into 100 parts and averaged. The 100 parts, each with a recording time of 1 s, were averaged. The averaged interferogram was fourfold zero filled to interpolate the spectrum. Portions of the mode-resolved structures at different CW operating wavelengths are shown in Fig. 8. The relative linewidth of the individual heterodyne teeth in the full spectral range is measured to be ~1.4 Hz. The dips in Fig. 8 are due to the absorption of the gas mixture; they are consistent with the absorption profiles computed from the HITRAN database. These results demonstrate the mutual coherence of our OMFCs at different injected CW wavelengths. The scheme can be further applied to other spectral regions by replacing the CW QCL at other operating wavelengths.

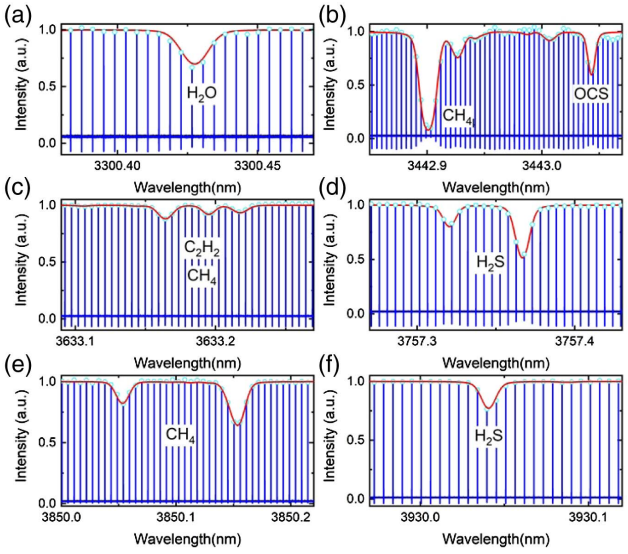

Fig. 8. Mode-resolved DCS spectra at different CW operating wavelengths. The red curves show the profiles computed from the HITRAN database using experimental parameters.

APPENDIX C: OCTAVE SPECTRUM OF OMFCS

Broadband mid-infrared DCS is of great importance for the parallel measurement of multiple gas species. The output spectral range of our OMFCs was limited by the phase-matching bandwidth of the fan-out grating PPLN. In this study, we achieved the spectral broadening of our OMFCs by introducing a cascade OPA process and combining the supercontinuum technique. As shown in Fig. 9(a), a long-pass filter (Thorlabs, FEL1300) was used to obtain the near-infrared idler after the CW-seeded OPA process, which was simultaneously generated along with the mid-infrared OMFC. The near-infrared idler was injected into a 1.5 m long polarization-maintaining fiber (PM1550), in which the pulse duration was compressed into ~40 fs [60]. It was then spliced into a 10 cm long HNLF to achieve supercontinuum broadening. The output, which served as the signal, was pumped by the residual pump energy in the next OPA process. Thus, the supercontinuum

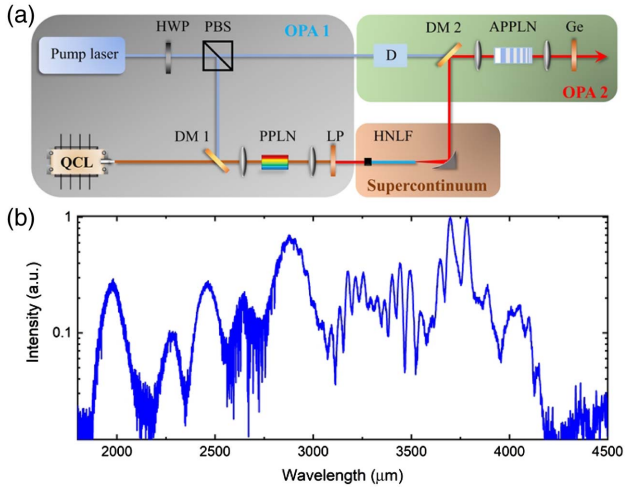

Fig. 9. (a) Schematic of the spectral broadening of the OMFC. The generated near-infrared idler after the OPA process, which was first spectrally broadened, served as the signal in the next OPA process. Broadband mid-infrared pulses were obtained when a chirped PPLN crystal was used in the OPA process. HWP, half-wave plate; PBS, polarizing beam splitter; DM, dichroic mirror; PPLN, periodically poled lithium niobate crystal; LP, long-pass filter; HNLF, highly nonlinear fiber; D, delay line; APPLN, aperiodically poled lithium niobate crystal; Ge, AR-coated germanium window. (b) Measured mid-infrared spectrum after the cascade OPA processes.

broadening of the near-infrared idler was achieved. The output, which served as the signal, was pumped by the residual pump energy in the next OPA process. A chirped PPLN crystal with a length of 25 mm was used during this process. The period is changed from 32.0 to 23.0 μm at steps of 0.1 μm. After the OPA process, a spectrum from 1.8 to 4.2 μm was generated as shown in Fig. 9(b). Further optimization of the structure can produce an octave spectrum [55]. We can infer that broad mid-infrared OMFCs can be directly generated by introducing well-designed PPLN waveguides during the OPA process.

APPENDIX D: FREQUENCY ACCURACY OF OMFCS

The frequency accuracy of the common mid-infrared CW seeds directly determined the frequency accuracy of our DCS. Here we used a mid-infrared wavelength meter (Bristol 771B, 0.75 pm accuracy) to measure the optical frequency of the two CW seeds. The frequency accuracy of the wavelength meter is guaranteed by continuous calibration with a built-in He–Ne laser. To further evaluate the inherent accuracy of the wavelength meter, the optical frequency of a near-infrared CW diode (1560 nm, OEwaves, linewidth ~10 Hz), referenced to a stabilized frequency comb [26], was initially measured. The calibration of the absolute frequency of the near-infrared comb locked by an f-$2f$ architecture was performed against a Rb clock. The measured standard deviation of the near-infrared CW laser was 9.4 MHz, recorded with an averaging single measurement time of ~0.4 s and a total measurement time of 30 min as shown in Fig. 10(a), which represents the $1-\sigma$ inherit frequency accuracy of our wavelength meter near 1560 nm. Subsequently, we used a mid-infrared wavelength meter to measure the frequencies of the CW ICL and QCL. It should be noted that the mid-infrared wavelength meter is more accurate in the longer wavelength region. The measured standard deviations of the frequency fluctuations of the QCL and ICL were ~3.5 MHz and ~5.0 MHz, respectively, as shown in Figs. 10(b) and 10(c). The frequency jumps in Fig. 10(b) can be due to mode hopping of the ICL. We can consider the frequency shifts of our two mid-infrared CW seeds to be almost less than 10 MHz at a measurement time of 30 s, which is comparable to the inherent frequency accuracy of the wavelength meter. Compared to the FWHM of the absorption lines in our experiment, the influence of the frequency shift of our mid-infrared CW seeds can be neglected for measuring gas concentration and components. In addition, the monitoring of the CW frequency in real-time during the experiment can effectively avoid the possible mode hopping of our CW seeds.

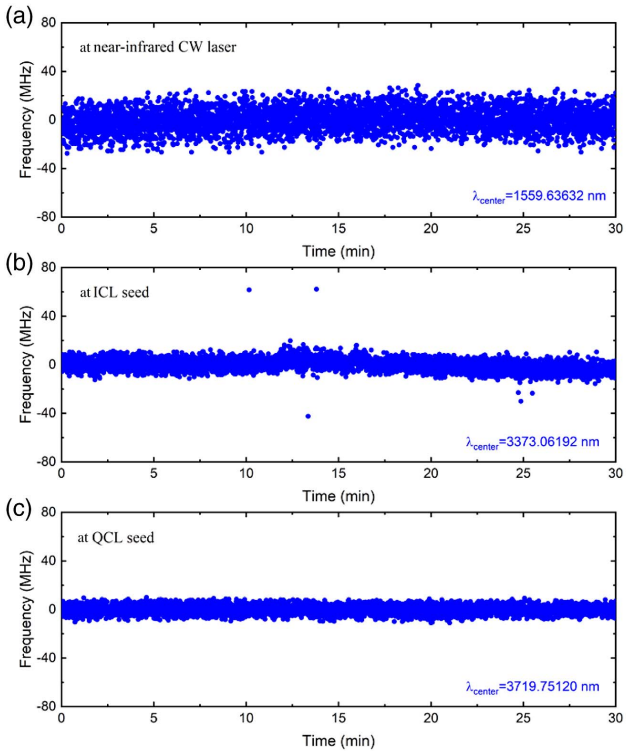

Fig. 10. Measured frequency stability of (a) near-infrared CW laser referenced to a fiber frequency comb, (b) mid-infrared CW ICL, and (c) QCL.

Funding. National Natural Science Foundation of China (11904105, 11874153, 11621404); National Key Research and Development Program of China (2018YFA0306301); China Postdoctoral Science Foundation funded project (2020M681223).

Disclosures. The authors declare no conflicts of interest.

†These authors contributed equally to this work.

REFERENCES

1. A. Rolland, P. Li, N. Kuse, J. Jiang, M. Cassinerio, C. Langrock, and M. E. Fermann, "Ultra-broadband dual-branch optical frequency comb with 10–18 instability," Optica **5**, 1070–1077 (2018).
2. T. W. Hänsch, "Nobel lecture: passion for precision," Rev. Mod. Phys. **78**, 1297–1309 (2006).
3. N. Picqué and T. W. Hänsch, "Frequency comb spectroscopy," Nat. Photonics **13**, 146–157 (2019).
4. A. V. Muraviev, V. O. Smolski, Z. E. Loparo, and K. L. Vodopyanov, "Massively parallel sensing of trace molecules and their isotopologues with broadband subharmonic mid-infrared frequency combs," Nat. Photonics **12**, 209–214 (2018).
5. G. Ycas, F. R. Giorgetta, K. C. Cossel, E. M. Waxman, E. Baumann, N. R. Newbury, and I. Coddington, "Mid-infrared dual-comb spectroscopy of volatile organic compounds across long open-air paths," Optica **6**, 165–168 (2019).
6. S. A. Meek, A. Hipke, G. Guelachvili, T. W. Hänsch, and N. Picqué, "Doppler-free Fourier transform spectroscopy," Opt. Lett. **43**, 162–165 (2018).
7. C. Wang, Z. Deng, C. Gu, Y. Liu, D. Luo, Z. Zhu, W. Li, and H. Zeng, "Line-scan spectrum-encoded imaging by dual-comb interferometry," Opt. Lett. **43**, 1606–1609 (2018).
8. E. Hase, T. Minamikawa, T. Mizuno, S. Miyamoto, R. Ichikawa, Y. Hsieh, K. Shibuya, K. Sato, Y. Nakajima, A. Asahara, K. Minoshima, Y. Mizutani, T. Iwata, H. Yamamoto, and T. Yasui, "Scan-less confocal phase imaging based on dual-comb microscopy," Optica **5**, 634–643 (2018).
9. M. Tamamitsu, K. Toda, H. Shimada, T. Honda, M. Takarada, K. Okabe, Y. Nagashima, R. Horisaki, and T. Ideguchi, "Label-free biochemical quantitative phase imaging with mid-infrared photothermal effect," Optica **7**, 359–366 (2020).
10. J. Mandon, G. Guelachvili, and N. Picqué, "Fourier transform spectroscopy with a laser frequency comb," Nat. Photonics **3**, 99–102 (2009).

11. K. Hiramatsu, Y. Luo, T. Ideguchi, and K. Goda, "Rapid-scan Fourier-transform coherent anti-Stokes Raman scattering spectroscopy with heterodyne detection," Opt. Lett. **42**, 4335–4338 (2017).
12. C. Gohle, B. Stein, A. Schliesser, T. Udem, and T. W. Hänsch, "Frequency comb vernier spectroscopy for broadband, high-resolution, high-sensitivity absorption and dispersion spectra," Phys. Rev. Lett. **99**, 263902 (2007).
13. S. A. Diddams, L. Hollberg, and V. Mbele, "Molecular fingerprinting with the resolved modes of a femtosecond laser frequency comb," Nature **445**, 627–630 (2007).
14. L. Rutkowski and J. Morville, "Broadband cavity-enhanced molecular spectra from Vernier filtering of a complete frequency comb," Opt. Lett. **39**, 6664–6667 (2014).
15. I. Coddington, N. Newbury, and W. Swann, "Dual-comb spectroscopy," Optica **3**, 414–426 (2016).
16. M. A. Abbas, Q. Pan, J. Mandon, S. M. Cristescu, F. J. M. Harren, and A. Khodabakhsh, "Time-resolved mid-infrared dual-comb spectroscopy," Sci. Rep. **9**, 17247 (2019).
17. T. Ideguchi, S. Holzner, B. Bernhardt, G. Guelachvili, N. Picqué, and T. W. Hänsch, "Coherent Raman spectro-imaging with laser frequency combs," Nature **502**, 355–358 (2013).
18. K. J. Mohler, B. J. Bohn, M. Yan, G. Mélen, T. W. Hänsch, and N. Picqué, "Dual-comb coherent Raman spectroscopy with lasers of 1-GHz pulse repetition frequency," Opt. Lett. **42**, 318–321 (2017).
19. J. T. Friedlein, E. Baumann, K. A. Briggman, G. M. Colacion, F. R. Giorgetta, A. M. Goldfain, D. I. Herman, E. V. Hoenig, J. Hwang, N. R. Newbury, E. F. Perez, C. S. Yung, I. Coddington, and K. C. Cossel, "Dual-comb photoacoustic spectroscopy," Nat. Commun. **11**, 3152 (2020).
20. B. Bernhardt, A. Ozawa, P. Jacquet, M. Jacquey, Y. Kobayashi, T. Udem, R. Holzwarth, G. Guelachvili, T. W. Hänsch, and N. Picqué, "Cavity-enhanced dual-comb spectroscopy," Nat. Photonics **4**, 55–57 (2010).
21. N. Hoghooghi, R. J. Wright, A. S. Makowiecki, W. C. Swann, E. M. Waxman, I. Coddington, and G. B. Rieker, "Broadband coherent cavity-enhanced dual-comb spectroscopy," Optica **6**, 28–33 (2018).
22. A. Hipke, S. A. Meek, T. Ideguchi, T. W. Hänsch, and N. Picqué, "Broadband Doppler-limited two-photon and stepwise excitation spectroscopy with laser frequency combs," Phys. Rev. A **90**, 011805 (2014).
23. S. Reinhardt, E. Peters, T. W. Hänsch, and T. Udem, "Two-photon direct frequency comb spectroscopy with chirped pulses," Phys. Rev. A **81**, 033427 (2010).
24. I. Coddington, W. C. Swann, and N. R. Newbury, "Coherent multiheterodyne spectroscopy using stabilized optical frequency combs," Phys. Rev. Lett. **100**, 013902 (2008).
25. G. Truong, E. M. Waxman, K. C. Cossel, E. Baumann, A. Klose, F. R. Giorgetta, W. C. Swann, N. R. Newbury, and I. Coddington, "Accurate frequency referencing for fieldable dual-comb spectroscopy," Opt. Express **24**, 30495–30504 (2016).
26. Z. Zhu, Y. Liu, D. Luo, C. Gu, L. Zhou, G. Xie, Z. Deng, and W. Li, "Tunable optical frequency comb from a compact and robust Er:fiber laser," High Power Laser Sci. Eng. **8**, e17 (2020).
27. Z. Chen, M. Yan, T. W. Hänsch, and N. Picqué, "A phase-stable dual-comb interferometer," Nat. Commun. **9**, 1 (2018).
28. Z. Chen, T. W. Hänsch, and N. Picqué, "Mid-infrared feed-forward dual-comb spectroscopy," Proc. Natl. Acad. Sci. USA **116**, 3454–3459 (2019).
29. Z. Chen, T. W. Hänsch, and N. Picqué, "Upconversion mid-infrared dual-comb spectroscopy," arXiv:2003.06930 (2020).
30. A. Schliesser, N. Picqué, and T. W. Hänsch, "Mid-infrared frequency combs," Nat. Photonics **6**, 440–449 (2012).
31. G. Ycas, F. R. Giorgetta, J. T. Friedlein, D. Herman, K. C. Cossel, E. Baumann, N. R. Newbury, and I. Coddington, "Compact mid-infrared dual-comb spectrometer for outdoor spectroscopy," Opt. Express **28**, 14740–14752 (2020).
32. G. Cerullo, A. Baltuška, O. D. Mücke, and C. Vozzi, "Few-optical-cycle light pulses with passive carrier-envelope phase stabilization," Laser Photon. Rev. **5**, 323–351 (2011).
33. S. C. Kumar, A. Esteban-Martin, T. Ideguchi, M. Yan, S. Holzner, T. W. Hänsch, N. Picqué, and M. Ebrahim-Zadeh, "Few-cycle, broadband, mid-infrared optical parametric oscillator pumped by a 20-fs Ti:sapphire laser," Laser Photon. Rev. **8**, L86–L91 (2014).
34. Y. Jin, S. M. Cristescu, F. J. M. Harren, and J. Mandon, "Femtosecond optical parametric oscillators toward real-time dual-comb spectroscopy," Appl. Phys. B **119**, 65–74 (2015).
35. M. Yu, Y. Okawachi, A. G. Griffith, N. Picqué, M. Lipson, and A. L. Gaeta, "Silicon-chip-based mid-infrared dual-comb spectroscopy," Nat. Commun. **9**, 1869 (2018).
36. L. A. Sterczewski, M. Bagheri, C. Frez, C. L. Canedy, I. Vurgaftman, and J. R. Meyer, "Mid-infrared dual-comb spectroscopy with room-temperature bi-functional interband cascade lasers and detectors," Appl. Phys. Lett. **116**, 141102 (2020).
37. G. Villares, A. Hugi, S. Blaser, and J. Faist, "Dual-comb spectroscopy based on quantum-cascade-laser frequency combs," Nat. Commun. **5**, 1–9 (2014).
38. B. Kuyken, T. Ideguchi, S. Holzner, M. Yan, T. W. Hänsch, J. V. Campenhout, P. Verheyen, S. Coen, F. Leo, R. Baets, G. Roelkens, and N. Picqué, "An octave-spanning mid-infrared frequency comb generated in a silicon nanophotonic wire waveguide," Nat. Commun. **6**, 5192 (2015).
39. Z. Zhao, B. Wu, X. Wang, Z. Pan, Z. Liu, P. Zhang, X. Shen, Q. Nie, S. Dai, and R. Wang, "Mid-infrared supercontinuum covering 2.0–16 μm in a low-loss telluride single-mode fiber," Laser Photon. Rev. **11**, 1700005 (2017).
40. E. Baumann, F. R. Giorgetta, W. C. Swann, A. M. Zolot, I. Coddington, and N. R. Newbury, "Spectroscopy of the methane ν_3 band with an accurate midinfrared coherent dual-comb spectrometer," Phys. Rev. A **84**, 062513 (2011).
41. F. Zhu, A. Bicer, R. Askar, J. Bounds, A. A. Kolomenskii, V. Kelessides, M. Amani, and H. A. Schuessler, "Mid-infrared dual frequency comb spectroscopy based on fiber lasers for the detection of methane in ambient air," Laser Phys. Lett. **12**, 095701 (2015).
42. G. Ycas, F. R. Giorgetta, E. Baumann, I. Coddington, D. Herman, S. A. Diddams, and N. R. Newbury, "High-coherence mid-infrared dual-comb spectroscopy spanning 2.6 to 5.2 μm," Nat. Photonics **12**, 202–208 (2018).
43. T. Ideguchi, T. Nakamura, Y. Kobayashi, and K. Goda, "Kerr-lens mode-locked bidirectional dual-comb ring laser for broadband dual-comb spectroscopy," Optica **3**, 748–753 (2016).
44. X. Zhao, T. Li, Y. Liu, Q. Li, and Z. Zheng, "Polarization-multiplexed, dual-comb all-fiber mode-locked laser," Photon. Res. **6**, 853–857 (2018).
45. G. Millot, S. Pitois, M. Yan, T. Hovhannisyan, A. Bendahmane, T. W. Hänsch, and N. Picqué, "Frequency-agile dual-comb spectroscopy," Nat. Photonics **10**, 27–30 (2015).
46. M. Yan, P. Luo, K. Iwakuni, G. Millot, T. W. Hänsch, and N. Picqué, "Mid-infrared dual-comb spectroscopy with electro-optic modulator," Light Sci. Appl. **6**, e17076 (2017).
47. C. Gu, Z. Zuo, D. Luo, Z. Deng, Y. Liu, M. Hu, and W. Li, "Passive coherent dual-comb spectroscopy based on optical-optical modulation with free running lasers," PhotoniX **1**, 7 (2020).
48. F. Cappelli, G. Campo, I. Galli, G. Giusfredi, S. Bartalini, D. Mazzotti, P. Cancio, S. Borri, B. Hinkov, J. Faist, and P. De Natale, "Frequency stability characterization of a quantum cascade laser frequency comb," Laser Photon. Rev. **10**, 623–630 (2016).
49. Q. Fu, L. Xu, S. Liang, P. C. Shardlow, D. P. Shepherd, S.-U. Alam, and D. J. Richardson, "High-beam-quality, watt-level, widely tunable, mid-infrared OP-GaAs optical parametric oscillator," Opt. Lett. **44**, 2744–2747 (2019).
50. C. Gu, Z. Zuo, D. Luo, D. Peng, Y. Di, X. Zou, L. Yang, and W. Li, "High-repetition-rate femtosecond mid-infrared pulses generated by nonlinear optical modulation of continuous-wave QCLs and ICLs," Opt. Lett. **44**, 5848–5851 (2019).
51. C. Gu, Z. Zuo, D. Peng, Y. Di, X. Zou, D. Luo, Y. Liu, and W. Li, "High-repetition-rate mid-IR femtosecond pulse synthesis from two mid-IR CW QCL-seeded OPAs," Opt. Express **28**, 27433–27442 (2020).
52. T. Ideguchi, A. Poisson, G. Guelachvili, N. Picque, and T. W. Hansch, "Adaptive real-time dual-comb spectroscopy," Nat. Commun. **5**, 3375 (2014).
53. D. Burghoff, Y. Yang, and Q. Hu, "Computational multiheterodyne spectroscopy," Sci. Adv. **2**, e1601227 (2016).
54. W. Chen, J. Fan, A. Ge, H. Song, Y. Song, B. Liu, L. Chai, C. Wang, and M. Hu, "Intensity and temporal noise characteristics in

femtosecond optical parametric amplifiers," Opt. Express **25**, 31263–31272 (2017).
55. L. Zhou, Y. Liu, H. Lou, Y. Di, G. Xie, Z. Zhu, Z. Deng, D. Luo, C. Gu, H. Chen, and W. Li, "Octave mid-infrared optical frequency comb from Er:fiber-laser-pumped aperiodically poled Mg:$LiNbO_3$," Opt. Lett. **45**, 6458–6461 (2020).
56. National Toxicology Program, "NTP 12th report on carcinogens," Rep. Carcinog. **12**, iii-499 (2011).
57. World Health Organization, *WHO Guidelines for Indoor Air Quality: Selected Pollutants* (World Health Organization, Regional Office for Europe, 2010), pp. 103–156.
58. C. Gu, X. Zou, Z. Zuo, D. Peng, Y. Di, Y. Liu, D. Luo, and W. Li, "Doppler velocimeter based on dual-comb absorption spectroscopy," Photon. Res. **8**, 1895–1903 (2020).
59. F. Adler, P. Masłowski, A. Foltynowicz, K. C. Cossel, T. C. Briles, I. Hartl, and J. Ye, "Mid-infrared Fourier transform spectroscopy with a broadband frequency comb," Opt. Express **18**, 21861–21872 (2010).
60. H. Timmers, A. Kowligy, A. Lind, F. C. Cruz, N. Nader, M. Silfies, G. Ycas, T. K. Allison, P. G. Schunemann, S. B. Papp, and S. A. Diddams, "Molecular fingerprinting with bright, broadband infrared frequency combs," Optica **5**, 727–732 (2018).